

## P6.34 CLEAR-SKY NARROWBAND ALBEDO VARIATIONS DERIVED FROM VIRS AND MODIS DATA

Sunny Sun-Mack, Yan Chen<sup>a</sup>, and Robert F. Arduini  
Science Application International Corporation, Hampton, VA USA 23666;

Patrick Minnis\*,  
Atmospheric Sciences, NASA Langley Research Center, Hampton, VA USA 23681

### 1. INTRODUCTION

A critical parameter for detecting clouds and aerosols and for retrieving their microphysical properties is the clear-sky radiance. Knowing the spatial and angular variability of clear-sky albedo is essential for predicting the clear-sky radiance at solar wavelengths. The Clouds and the Earth's Radiant Energy System (CERES) Project (Wielicki et al. 1998) uses the visible (VIS; 0.63  $\mu\text{m}$ ) and near-infrared (NIR; 1.6 or 2.13  $\mu\text{m}$ ) channels available on same satellites as the CERES scanners. Another channel often used for cloud and aerosol, and vegetation cover retrievals is the vegetation (VEG; 0.86- $\mu\text{m}$ ) channel that has been available on the Advanced Very High Resolution Radiometer (AVHRR) for many years.

Generally, clear-sky albedo for a given surface type is determined for conditions when the vegetation is either thriving or dormant and free of snow. Snow albedo is typically estimated without considering the underlying surface type. The albedo for a surface blanketed by snow, however, should vary with surface type because the vegetation often emerges from the snow to varying degrees depending on the vertical dimensions of the vegetation. For example, a snow-covered prairie will probably be brighter than a snow-covered forest because the snow typically falls off the trees exposing the darker surfaces while the snow on a grassland at the same temperatures will likely be continuous and, therefore, more reflective. Accounting for the vegetation-induced differences should improve the capabilities for distinguishing snow and clouds over different surface types and facilitate improvements in the accuracy of radiative transfer calculations between the snow-covered surface and the atmosphere, eventually leading to improvements in models of the energy budgets over land.

Sun-Mack et al. (1999) developed models of spectral clear-sky snow-free albedo for CERES using the Visible Infrared Scanner (VIRS) on the Tropical Rainfall Measuring Mission (*TRMM*) satellite. The VIRS takes measurements at all times of day over a given region between 37°N and 37°S during a period of 46 days providing the opportunity to derive albedo values over all solar zenith angles (SZA). The VIRS data gave a baseline snow-free albedo dataset for low-latitude

areas but provides no information on temperate and polar regions. CERES also operates on the Terra and Aqua satellites using the Moderate Resolution Imaging Spectroradiometer (MODIS) to derive cloud properties. Sun-Mack et al. (2003) performed an initial analysis of clear-sky albedo for both snow-free and snow-covered conditions for CERES cloud retrievals from MODIS data. This paper presents a more complete analysis of the CERES spectral clear-sky reflectances to determine the variations in clear-sky top-of-atmosphere (TOA) albedos for both snow-free and snow-covered surfaces for four spectral channels using data from *Terra* and *Aqua*. The results should be valuable for improved cloud retrievals and for modeling radiation fields.

### 2. DATA & METHODOLOGY

*Terra* and *Aqua* began producing MODIS imagery in late February 2000 and early summer 2002, respectively. Except for the 1.6- $\mu\text{m}$  channel, the *Aqua* MODIS sensors are working well. For CERES, every other 1-km MODIS pixel and 3 out of four scan lines are skipped to minimize processing time and data storage. Each MODIS pixel is initially classified as clear or cloudy using updated versions of the CERES classification schemes that rely on the radiances measured by the VIS, NIR, 3.7, 11, and 12- $\mu\text{m}$  channels (Trepte et al., 1999, 2002). The radiances are compared with predicted clear-sky radiances based on empirical estimates of spectral clear-sky albedo and on skin temperatures from the Global Modeling Assimilation Office GEOS 4.03 (DAO, 1997) reanalyses adjusted using empirical estimates of spectral surface emissivity (Chen et al. 2002) and atmospheric absorption calculated with the GEOS vertical profiles of temperature and humidity.

All clear pixels during an overpass are averaged into the appropriate 1° region, which is assigned a single surface type  $K$  defined by the International Geosphere Biosphere Programme (IGBP). For each region, the mean observed clear-sky reflectance for a given overpass is

$$\rho_{\lambda} = \rho_{\lambda}(K; LAT, LON; \mu_o, \mu, \psi) \quad (1)$$

where  $\lambda$  is the wavelength,  $K$  is the International Geosphere Biosphere Programme (IGBP) surface type (see Table 1),  $LAT$  and  $LON$  are the center latitude and longitude of the region, respectively,  $\mu_o$  and  $\mu$  are the cosines of SZA and viewing zenith angle (VZA), respec-

\*Corresponding author address: P. Minnis, MS 420  
NASA Langley Res. Ctr., Hampton, VA 23681  
email: p.minnis@nasa.gov;

Table 1: Surface type categories and overhead sun albedos from TRMM VIRS and *Terra* MODIS (Summer).

K	IGBP Type	VIRS $a_o$		MODIS $a_o$			Snow Type	
		0.65 $\mu\text{m}$	1.64 $\mu\text{m}$	0.64 $\mu\text{m}$	0.87 $\mu\text{m}$	1.62 $\mu\text{m}$		2.13 $\mu\text{m}$
1	evergreen needleleaf	0.092	0.209	0.080	0.292	0.192	0.095	forest
2	evergreen broadleaf	0.100	0.196	0.084	0.329	0.182	0.077	forest
3	deciduous needleleaf	-----	-----	0.080	0.338	0.195	0.097	forest
4	deciduous broadleaf	0.097	0.235	0.083	0.369	0.220	0.098	forest
5	mixed forest	0.092	0.217	0.080	0.334	0.200	0.092	forest
6	closed shrubland	0.138	0.300	0.149	0.254	0.308	0.192	grass
7	open shrubland	0.226	0.411	0.234	0.303	0.397	0.311	grass
8	woody savanna	0.117	0.260	0.107	0.277	0.238	0.123	grass
9	savanna	0.153	0.328	0.148	0.287	0.313	0.189	grass
10	grassland	0.172	0.356	0.173	0.296	0.346	0.253	grass
11	permanent wetland	0.085	0.125	0.083	0.189	0.148	0.082	coast
12	cropland	0.129	0.252	0.120	0.300	0.250	0.145	grass
13	urban	0.132	0.235	0.117	0.253	0.208	0.120	grass
14	mixed grass-forest	0.132	0.274	0.120	0.301	0.263	0.155	grass
15	snow-ice	0.294	0.157	0.329	0.321	0.148	0.121	snow-ice
16	desert, barren/sparse vegetation	0.313	0.544	0.323	0.404	0.518	0.454	desert
17	water	0.059	0.027	0.057	0.037	0.026	0.019	water
18	tundra	0.230	0.363	0.219	0.305	0.355	0.340	desert
19	coastline (10-90% water)	0.125	0.191	0.109	0.218	0.166	0.107	coast

tively, and  $\psi$  is the relative azimuth angle. These instantaneous pixel-level and regional mean clear-sky reflectances are the fundamental datasets used here.

Clear-sky reflectance consists of the radiation reflected by the atmosphere and the surface. The primary atmospheric effects on the reflected VIS (0.65  $\mu\text{m}$ ) radiances are Rayleigh and aerosol scattering and ozone absorption, while water vapor absorption and aerosols are the primary attenuators in the NIR channels. The effects of water vapor and aerosols are generally minor except for aerosols over ocean. Minnis et al. (2002) found that the VIRS VIS reflectance is up to 0.02 greater than MODIS at low values. This discrepancy can be explained mostly by the Rayleigh scattering differences within the two spectral intervals.

Each reflectance is converted to albedo  $\alpha_\lambda$  in the following manner,

$$\alpha_\lambda = \rho_\lambda(K; LAT, LON; \mu_o, \mu, \psi) / \chi_\lambda(K; \mu_o, \mu, \psi), \quad (2)$$

where  $\chi_\lambda$  is the normalized bidirectional reflectance distribution function (BRDF) for the particular surface type and wavelength. Over water surfaces, the BRDF values for all wavelengths are taken from an empirical model based on geostationary satellite data (Minnis and Harrison, 1984). An broadband empirical model (Suttles et al., 1988) is used for all wavelengths over barren desert scenes. The snow BRDFs for each were developed from calculations using an adding-doubling radiative transfer model. The snow surface was assumed to be a layer of randomly oriented, hexagonal

ice crystals having a length to width ratio L/D of 750 $\mu\text{m}$ /160 $\mu\text{m}$  with an optical depth of 1000 (Takano et al., 1989). The model BRDFs at the top of the atmosphere were computed using a radiative transfer model incorporating the May 22 (clear-sky) Arctic atmosphere from the European Center for Medium-Range Weather Forecasting analysis and a correlated  $k$ -distribution method (Kratz, 1995). The snow BRDFs were used for permanent ice/snow surfaces and any other scene classified as snow covered. For  $K = 19$ , an empirical coastal model was used for all wavelengths. A broadband empirical land model from Suttles et al. (1988) was used for the VIS channel over all remaining surface types ( $K = 1-14, 18$ ). BRDFs for the other channels and remaining surface types were derived from aircraft measurements taken at 0.877, 1.66, and 2.13  $\mu\text{m}$  for four distinct surfaces (Kriebel et al., 1978). The coniferous forest models were used for all forest types ( $K = 1, 5$ ), while bog was used for  $K = 11, 18$ , and 19. The savanna data were used for  $K = 6, 7, 8, 9$ , and 13 and the pasture results were used for  $K = 10, 12$ , and 14.

Instantaneous TOA albedos for each pixel were then averaged for every 0.1  $\mu_o$  interval to examine the SZA dependence. The means for the 19 surface types were further averaged into 6 snow types based on vegetation or amount of water surface as listed in Table 1. The analyses have been completed for 3 years of *Terra* (2000 – 2002) and only 2 months of *Aqua* data, July and December 2002. The mean TOA overhead-sun albedo  $\alpha_o$  was computed from the SZA-binned albedo

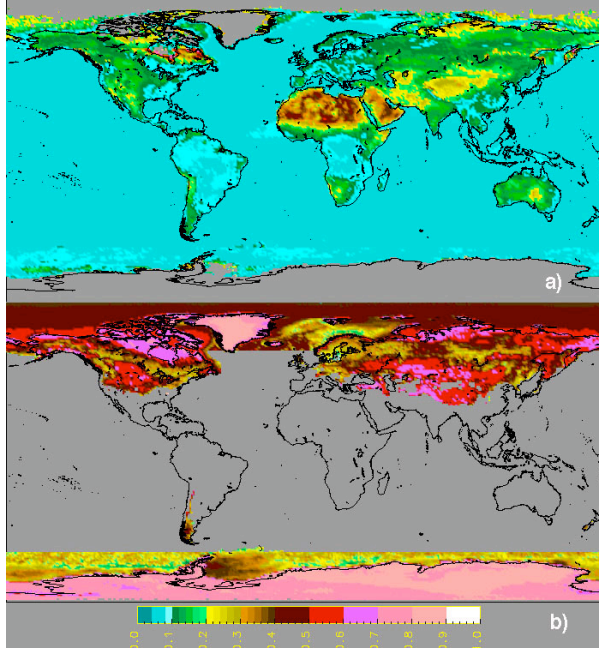


Fig. 1. Mean MAM clear-sky overhead-sun Terra MODIS 0.63- $\mu\text{m}$  albedos, 2000-2002: (a) no snow, (b) only areas with snow.

for each region and type using a set of empirical directional reflectance models (DRMs) from VIRS for 0.65 and 1.6- $\mu\text{m}$  data (Sun-Mack et al. (1999, Chen et al., 2002). The former and latter DRMs were used also for 0.87 and 2.1  $\mu\text{m}$ , respectively. The results are listed in Table 1 for snow-free conditions using VIRS data from summer months (1998-2001) and *Terra* data from summer months (2000-2002). The VIRS 1.6- $\mu\text{m}$  albedos agree with their MODIS counterparts within 1% and VIRS 0.6  $\mu\text{m}$  albedos agree with MODIS to within 0.4%.

### 3. RESULTS AND DISCUSSION

Figure 1 shows the distribution of mean 0.63- $\mu\text{m}$  clear-sky albedos for snow-free and snow-covered areas during the 2000-2002 boreal spring (MAM) seasons from *Terra* data. Most of the snow-covered areas are confined to latitudes poleward of 60°S in the Southern Hemisphere with the exception of a few areas in the Andes. In the Northern Hemisphere, the snow line extends as far south as 30°N over the Tibetan Plateau. The VIS albedos increase as a result of snow cover and are greatest over the land areas and adjacent waters with permanent coverage. The lowest albedos for snow-covered land occur over the regions with boreal forests in Canada and Siberia while greater values are found over the less-vegetated areas such as tundra and grasslands. The relatively sharp lines at the 60° latitudes in Fig. 1b are artifacts of the cloud mask, which switches to a polar-oriented algorithm at 60°. It results in more snow detection at the higher latitudes.

The NIR albedos behave differently for snow as seen in Fig. 2 for the 2.13- $\mu\text{m}$  channel. When snow

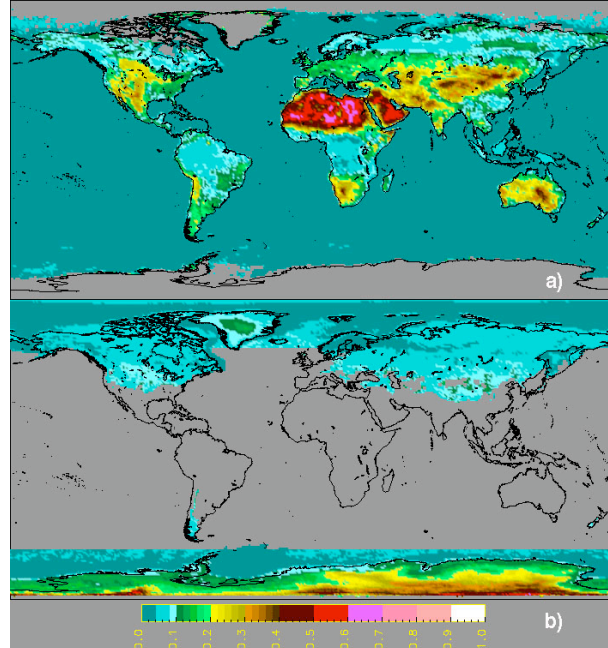


Fig. 2. Same as Fig. 1, except for 2.1  $\mu\text{m}$ .

covers the surface, the NIR albedos typically decrease. Over Asia and North America, the NIR albedos reach 0.3 or greater when they are free of snow. When snow is added, the 2.1- $\mu\text{m}$  albedos drop to values below 0.1. Similar to the VIS channel, the NIR albedos are greatest for land areas with permanent snow with maximum values of 0.5 in central Antarctica.

The mean albedos for all four seasons for permanent snow-ice, IGBP category 15, are plotted in Fig. 3 to provide a reference point for the snow albedos over other surface types. The seasons are defined relative to the Northern Hemisphere. These datasets show lower albedos at large values of  $\mu_o$  for the VIS and VEG channels compared to the values for  $\mu_o < 0.7$ . The higher VIS values are consistent with those from theoretical calculations that indicate reflectances varying between 0.82 and 0.88 for pure snow surfaces (Trepte et al., 2002). The lower values at large  $\mu_o$  are probably mostly from midlatitude and subtropical glaciers that may not completely cover the 1° regions and may be dirtier than their polar counterparts. Additionally, at the smaller SZAs, more surface melting may occur causing a reduction in the albedo. The NIR (1.6 and 2.1  $\mu\text{m}$ ) albedos in Fig. 3 are considerably lower due to the strong absorption by the large snow crystals. They increase at larger values of  $\mu_o$ , further reinforcing the presence of vegetated or bare rock areas within the 1° regions.

The VIS albedos tend to peak around  $\mu_o = 0.6$ . The rapid decrease for increasing  $\mu_o$  is probably due to the contamination effect mentioned above while the gradual drop for smaller values of  $\mu_o$  might be due to enhanced ozone absorption with the increasing path length. This idea is supported by the gradual increase in VEG albedo, which is unaffected by ozone, with decreasing

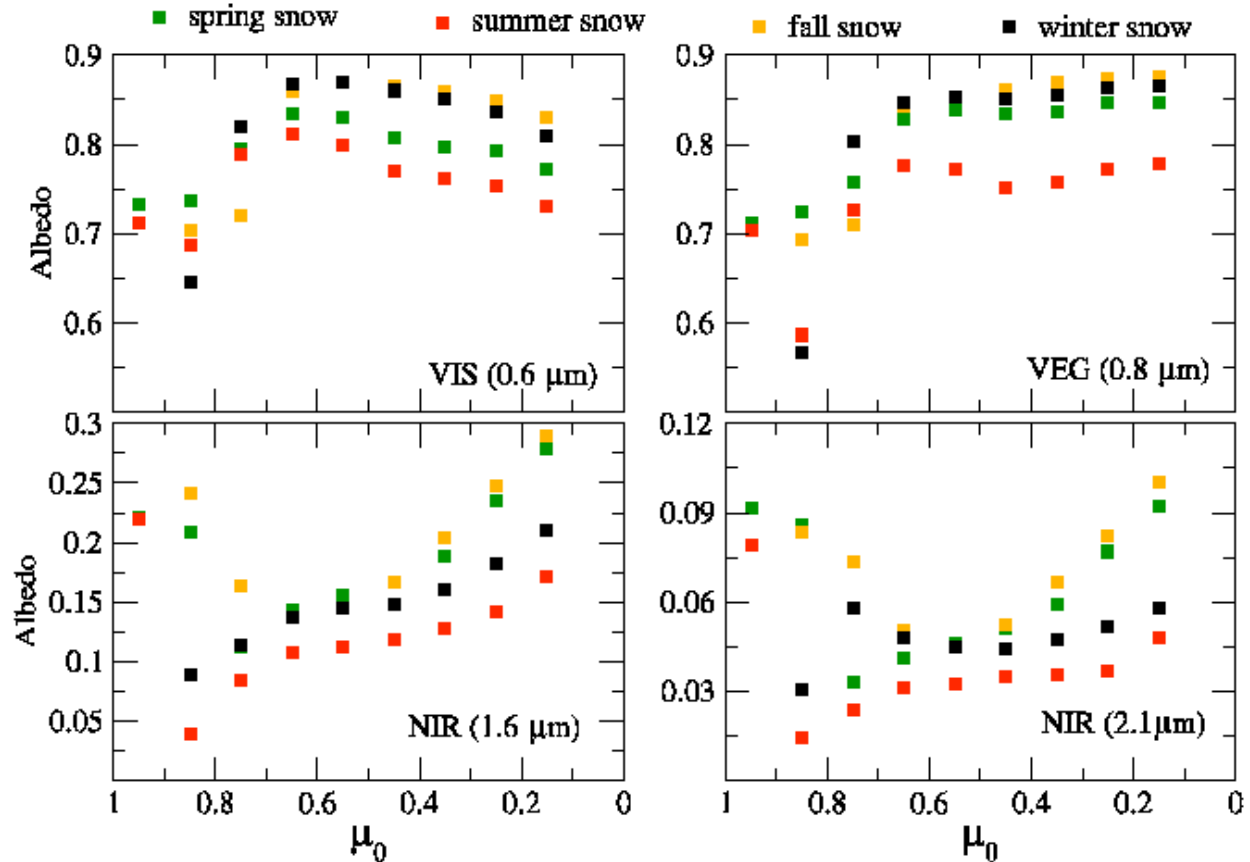


Fig. 3. Mean seasonal albedos over areas with permanent snow and ice from Terra MODIS, 2000-2002.

$\mu_0$ . The NIR albedos also rise with dropping  $\mu_0$ . All of the albedos are least during the boreal summer mainly as a result of losing the Antarctica data to the polar night. Conversely, they are greatest during the winter because most of the data are from the southernmost continent. Mean albedos were computed for the same permanent snow-ice scenes using both *Terra* and *Aqua* data for July 2002 and December 2002 separately. When sampling was significant within a given SZA bin, the albedos agreed to within a few percent for all 3 operating channels common to both sensors (not shown). Similar consistency between the two satellite results was found over all surfaces. Hereafter, only results from 2000-2002 *Terra* data are presented.

Figure 4 shows the albedos over forested land for snow-free and snow-covered conditions. Without snow, VIS albedo increases with SZA while the VEG albedo decreases slightly for  $\mu_0 > 0.6$  and increases slightly for  $\mu_0 < 0.6$ . Snow-free forests are darkest in the VIS band during summer, presumably because of the large number of boreal forest regions that are sampled. The forest VIS and VEG mean albedos increase by 2-5 times and are much noisier when they are blanketed with snow. The VIS albedo increases with SZA during spring but decreases during fall and is relatively constant during the remaining seasons. The VIS values average around 0.50, while the VEG albedos range

from 0.48 to 0.65 depending on the mean albedo of the snow-free background. These snow-scene albedos are 40% less than those for the permanent snow-ice areas, indicating that the vertical structure of vegetation reduces the snow coverage and therefore reduces the impact of snow on the albedo. The opposite behavior occurs for the NIR channels with the snow-free albedos exceeding their counterparts with snow. The NIR mean albedos are noisier for snow-free conditions than for snow-covered scenes.

Over grass and shrub lands (Fig. 4), all of the spectral albedos are greater than those over forests. The VIS albedos tend to increase with SZA, and VEG is relatively flat with SZA for snow-free conditions. The mean VIS and VEG albedos in snow-covered conditions are roughly 0.60 and 0.68, respectively. The NIR snow-free albedos over grass are double the values for their snow-covered counterparts. Variations of albedo with SZA for all of the snow albedos in Fig. 5 are probably influenced by the greater insolation and by increased vegetation contamination at greater values of  $\mu_0$ .

In desert and tundra areas, the VEG and VIS albedos are much closer than over the other vegetated areas (not shown). For snow-free conditions, the NIR albedos all decrease dramatically between  $\mu_0 = 0.75$  and 0, and the VIS and VEG albedos remain relatively

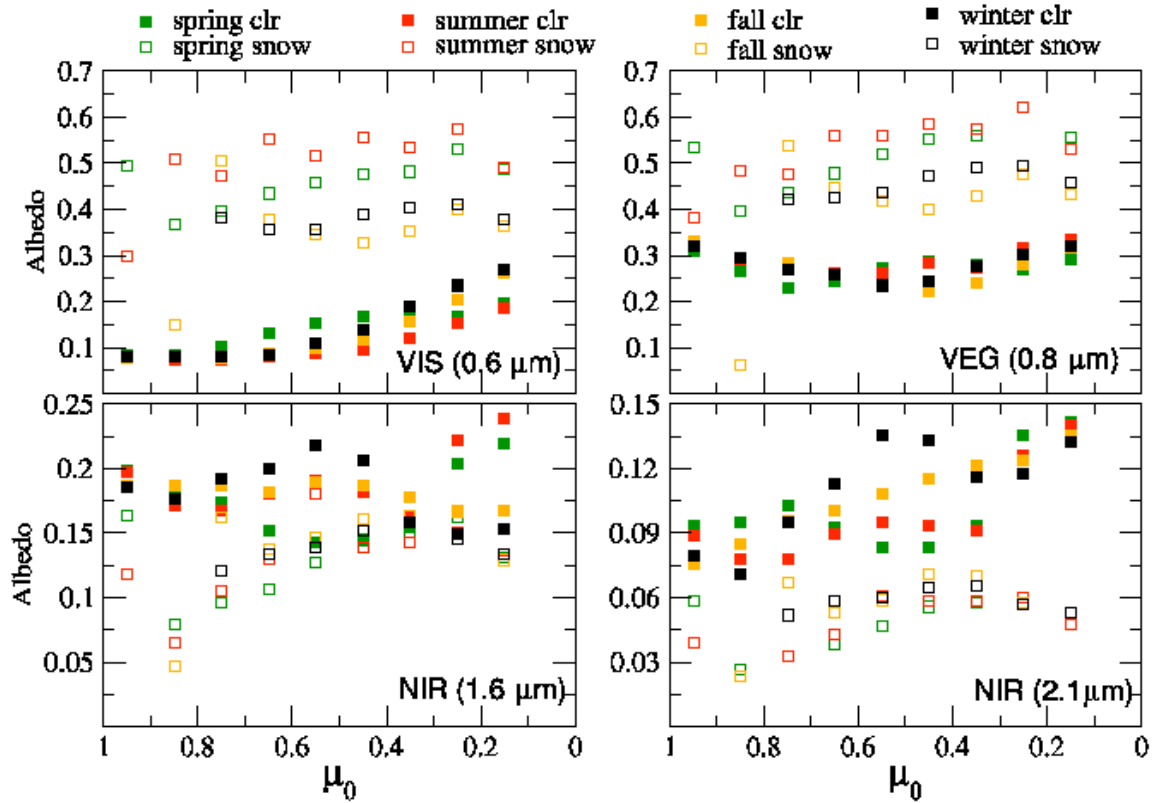


Fig. 4. Same as Fig. 3, except for forested regions.

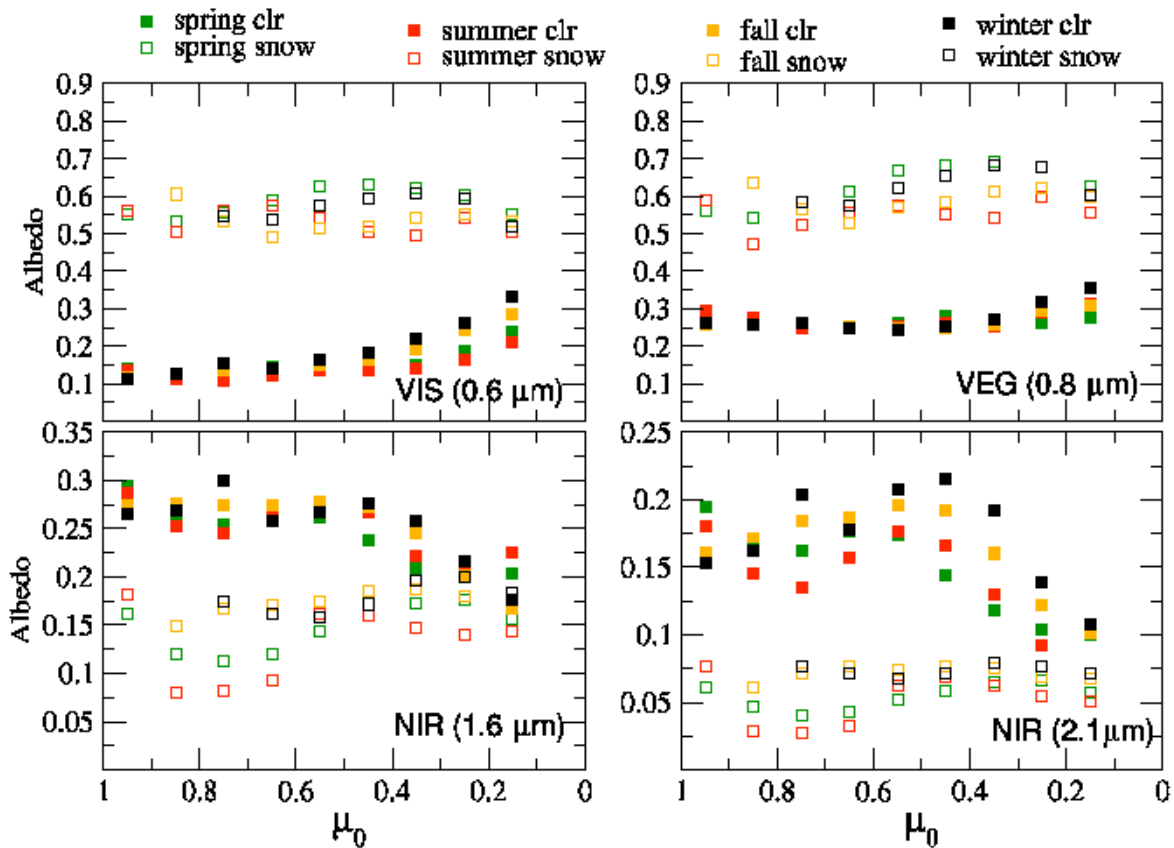


Fig. 5. Same as Fig. 3, except for grass and shrub lands.

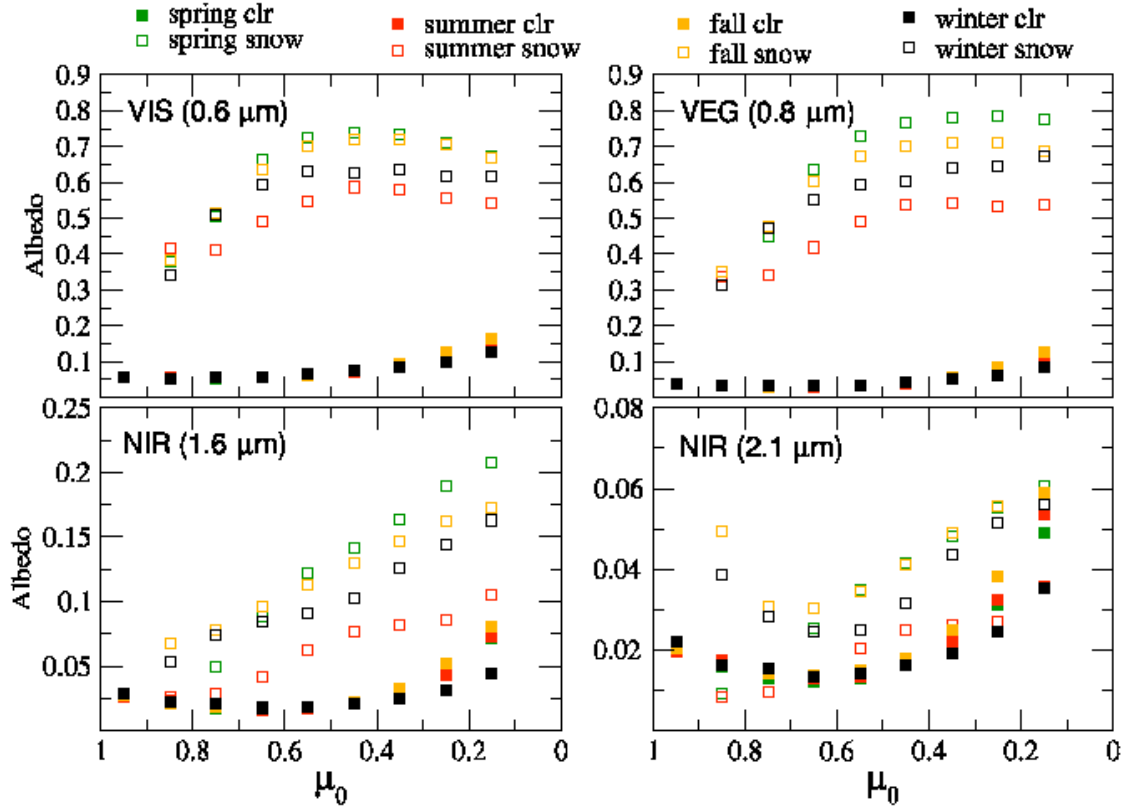


Fig. 6. Same as Fig. 3, except for water surfaces.

constant for all values of  $\mu_o$ . This dependence is due to the changing nature of the scenes with latitude. At low latitudes (large  $\mu_o$ ), the very bright deserts in North Africa and the Arabian Peninsula dominate the averages (Fig. 1), while at higher latitudes, darker deserts and slightly vegetated tundra prevail. Despite the great variations in background albedos when no snow is present, the albedos are relatively unchanged with SZA when snow is present. Both the VIS and VEG albedos change smoothly from  $\sim 0.6$  to  $0.8$ .

Over ocean (Fig. 6), the albedos appear to behave more predictably than over land surfaces due to a combination of greater sampling and surface homogeneity than over land. Compared to land areas, the albedos over the temporarily snow and ice-covered waters (Fig. 6) are much closer to those for the permanent snow-ice areas except at the higher values of  $\mu_o$ . At  $\mu_o = 0.6$ , the VEG and VIS albedos are lower due to melt ponds and to pixels only partially covered with ice (e.g., floes or icebergs). Unlike the land areas, snow raises the NIR albedos over ocean by factors of 4 or 5 at  $1.6 \mu\text{m}$  and factors of 2 at  $2.1 \mu\text{m}$ . The albedos over coastal areas are between those over ocean and land (not shown).

Understanding the differences in the albedos for various surface types requires comparisons at the same SZA. When the DRM is known for each surface type, it is possible to determine  $\alpha_o$  and have a basis for comparison (e.g., Table 1). However, such DRMs are

not currently available for the different land surfaces covered by snow. The latitude-dependent SZA sampling by single sun-synchronous satellites, for the most part, precludes their derivation (Fig. 7). To overcome these sampling difficulties, the mean albedos were computed for each category using the  $\mu_o$ -weighted values for  $\mu_o$  between 0.55 and 0.25, the angles where all categories have values. The mean  $\mu_o$  corresponds to SZA =  $66.4^\circ$ . Table 2 summarizes the resulting mean values. The maximum snow-free land albedos are found for the VEG channel while the minimum values occur at  $2.1 \mu\text{m}$ . Ocean albedo is greatest at  $0.65 \mu\text{m}$  and least at  $2.1 \mu\text{m}$ . When snow covers the various surfaces, the VIS

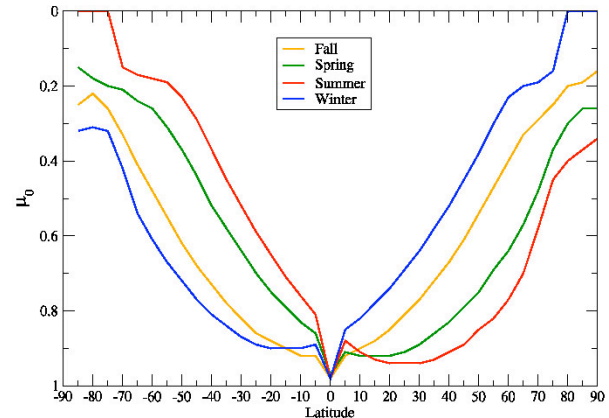


Fig. 7. Seasonal variation of mean  $\mu_o$  at Terra overpass times.

Table 2: Mean Terra MODIS clear-sky albedos at SZA = 66.4° for boreal winter months, 2000 – 2002.

Surface type	snow -free				snow-covered			
	0.65 $\mu\text{m}$	0.87 $\mu\text{m}$	1.6 $\mu\text{m}$	2.1 $\mu\text{m}$	0.65 $\mu\text{m}$	0.87 $\mu\text{m}$	1.6 $\mu\text{m}$	2.1 $\mu\text{m}$
forest	0.134	0.244	0.206	0.133	0.388	0.472	0.152	0.064
grass	0.184	0.252	0.276	0.215	0.595	0.654	0.172	0.071
desert	0.272	0.330	0.382	0.324	0.618	0.661	0.182	0.082
coast	0.137	0.159	0.129	0.087	0.553	0.626	0.158	0.060
ocean	0.075	0.042	0.021	0.016	0.629	0.604	0.102	0.032
snow-ice	0.152	0.128	0.035	0.024	0.860	0.852	0.148	0.044

and VEG albedos increase according to the vertical structure of the vegetation. The values over land are least for the forest and greatest for smoother desert and tundra surfaces with grass-shrub vegetation in the middle. Once snow collects on an ice covered ocean surface, however, the VIS/VEG albedos exceed those over land and are closest to the those for areas permanently covered by snow and ice. However, some of the areas that are classified as permanent snow-ice actually undergo melting exposing the underlying surfaces. These surfaces are generally dark and probably consist of ocean and rock. Thus, all of the snow-free albedos are between those for ocean and coastline. The mean NIR albedos for the snow-covered surfaces are remarkably invariant with surface type, especially at 1.6  $\mu\text{m}$ . This behavior was implicit in the development of the snow detection algorithm, which relies heavily on the reflectance at 3.7  $\mu\text{m}$ , but was never tested. It is likely that the 3.7- $\mu\text{m}$  albedos behave in a similar manner but are probably less than those at the four wavelengths considered here. Over the land areas, the 2.1- $\mu\text{m}$  snow albedos are about 25% greater than the permanent snow-ice value indicating some influence of the vegetation on the albedo.

#### 4. CONCLUSIONS

The seasonal results shown here capture the variability of snow albedo with surface type for spectral channels commonly used for Earth and atmospheric remote sensing. The vertical structure of vegetation apparently has a significant influence on the snow albedos and should be taken into account for both remote sensing and radiation budget purposes. It is clear that the combinations of the various channels can be refined to further improve the discrimination between scenes with clouds and those with snow on the surface. Future studies will take advantage of the large clear and cloudy database continuing to be developed by CERES from all of the *TRMM*, *Terra*, and *Aqua* imager datasets. Those datasets should improve the statistics, including standard deviations, for all of the surface types and solar zenith angles. Because the spectral albedos vary for the IGBP types within the “snow categories” used here, albedo statistics should also be derived for each

individual IGBP type. Finally, it should be noted that the BRDFs used here are not necessarily optimal for each channel and surface type. While the average albedos derived here may not be too sensitive to the particular BRDF because they are the result of radiances taken at many different viewing conditions, it is desirable to repeat the analyses if improved spectral BRDFs become available.

#### ACKNOWLEDGMENTS

This research is sponsored by the NASA Earth Enterprise System through the CERES Program.

#### REFERENCES

- Chen, Y., S. Sun-Mack, Q. Z. Trepte, P. Minnis, and D. F. Young, 2002: Solar zenith angle variation of clear-sky narrowband albedos derived from VIRS and MODIS. *Proc. 11<sup>th</sup> AMS Conf. Atmos. Rad.*, Ogden, UT, June 3-7, 152-155.
- Chen, Y., S. Sun-Mack, P. Minnis, D. F. Young, and W. L. Smith, Jr., 2002: Surface spectral emissivity derived from MODIS data. *Proc. SPIE Conf. Optical Remote Sensing of Atmos. and Clouds III*, Hangzhou, China, Oct. 23-27, **4891**, 361-369.
- DAO, 1997: GEOS-3 Data Assimilation System Architectural Design. *DAO Office Note 97-06*. Data Assimilation Office, Goddard Space Flight Center, Greenbelt, MD 20771.
- Kratz, D.P., 1995: The correlated-k distribution technique as applied to the AVHRR channels. *J. Quant. Spectrosc. Radiat. Transfer*, **53**, 501-510.
- Kriebel, K. T., 1978: Measured spectral bidirectional reflectance properties of vegetated surfaces. *Appl. Opt.*, **17**, 253-259.
- Minnis, P. and E. F. Harrison, 1984: Diurnal variability of regional cloud and clear-sky radiative parameters derived from GOES data. Part III: November 1978 radiative parameters. *J. Climate Appl. Meteor.*, **23**, 1032-1051.
- Minnis, P., L. Nguyen, D. R. Doelling, D. F. Young, W. F. Miller, and D. P. Kratz, 2002: Rapid calibration of operational and research meteorological satellite imagers, Part I: Evaluation of research satellite



- visible channels as references. *J. Atmos. Oceanic Technol.*, **19**, 1233-1249.
- Sun-Mack, S., Y. Chen, T. D. Murray, P. Minnis, and D. F. Young, 1999: Visible clear-sky and near-infrared surface albedos derived from VIRS for CERES. *Proc. AMS 10<sup>th</sup> Conf. Atmos. Rad.*, Madison, WI, June 28–July 2, 422-425.
- Sun-Mack, S., P. Minnis, Y. Chen, and R. F. Arduini, 2003: Clear-sky narrowband albedos derived from VIRS and MODIS. *SPIE 10<sup>th</sup> Intl. Symp Remote Sens., Conf. Remote Sens. Clouds and Atmos.*, Barcelona, Spain, September 8-12, 101-109.
- Suttles, J. T., R. N. Green, P. Minnis, G. L. Smith, W. F. Staylor, B. A. Wielicki, I. Walker, D. F. Young, V. R. Taylor, and L. L. Stowe, 1988: Angular radiation models for Earth-atmosphere system, Vol. 1, Shortwave radiation. *NASA RP-1184*, 144 pp.
- Takano, Y. and K. N. Liou, 1989: Radiative transfer in cirrus clouds: I single scattering and optical properties of oriented hexagonal ice crystals. *J. Atmos. Sci.*, **46**, 3-20.
- Trepte, Q., Y. Chen, S. Sun-Mack, P. Minnis, D. F. Young, B. A. Baum, and P. W. Heck, 1999: Scene identification for the CERES cloud analysis subsystem. *Proc. AMS 10<sup>th</sup> Conf. Atmos. Rad.*, Madison, WI, June 28 – July 2, 169-172.
- Trepte, Q., R. F. Arduini, Y. Chen, S. Sun-Mack, P. Minnis, D. A. Spangenberg, and D. R. Doelling, 2001: Development of a daytime polar cloud mask using theoretical models of near-infrared bidirectional reflectance for ARM and CERES. *Proc. AMS 6th Conf. on Polar Meteorology and Oceanogr.*, San Diego, CA, May 14-18, 242-245.
- Trepte, Q. Z., P. Minnis, and R. F. Arduini, 2002: Daytime and nighttime polar cloud and snow identification using MODIS. *Proc. SPIE Conf. Optical Remote Sensing of Atmos. and Clouds III*, Hangzhou, China, Oct. 23-27, **4891**, 449-459.
- Wielicki, B. A., et al., 1998: Clouds and the Earth's Radiant Energy System (CERES): Algorithm overview. *IEEE Trans. Geosci. Remote Sens.*, **36**, 1127-1141.